ORIGINAL ARTICLE

Chemical composition of oscillatory zoned garnets from the large-scale Mengya'a Pb–Zn skarn deposit: implications for fluid physicochemical conditions and formation

Yan Zhang[1] · Cuihua Chen[1] · Yulong Yang[1] · Xuhao Kang[1] · Ying Gu[1] · Xiang Lai[1] · Xiaojie Chen[1]

Abstract The Mengya'a Lead–zinc deposit is a large skarn deposit in the north of the eastern segment of Gangdese metallogenic belt. The garnet is the main altered mineral in the Mengya'a area. The color of the garnet varies from chartreuse to dark yellow brown and to russet. The brown garnet (Grt1) is related to pyrrhotite and chalcopyrite, and the green garnet (Grt2) is associated with lead–zinc mineralization. LA-ICP-MS is the induced coupled plasma mass spectrometry. This paper has used this technique to investigate Grt1 and Grt2. Grt1 develops core–rim textures with strong oscillation zone occurring in rim, whereas Grt2 lacks core–rim textures and featured by oscillation zone. LA–ICP–MS analysis shows that garnets of Mengya'a are rich in CaO (29.90–37.52 %) and FeO (21.17–33.35 %), but low in Al_2O_3 (0.05–4.85 %). The calculated end members belong to grandite (grossular–andradite) garnets andradite. The negative Al (IV) versus Fe^{3+}, positive Al (IV) versus total Al stoichiometric number, the positive Al (IV) versus Fe^{3+}, and the negative Al (IV) versus total REE, all indicate that the substitution of REEs in garnets is controlled by YAG. All Garnets are depleted in large lithophile elements (e.g., Rb = 0.00–4.01 ppm, Sr = 0.03–8.56 ppm). The total REE in Grt1 core is high ($\sum$REE = 233–625 ppm), with HREE enriched pattern (LREE/HREE = 0.33–1.69) and weak negative Eu anomalies (δEu = 0.21–0.47). In contrast, the total REEs in the Grt1 rim and Grt2 are low (ΣREE = 12.4–354 ppm; ΣREE = 21.0–65.3 ppm), with LREE enriched pattern (LREE/HREE = 0.54–34.4; LREE/HREE = 11.4–682) and positive Eu anomalies (δEu = 0.35–27.2; δEu = 1.02–30.7). After data compilation of garnet chemicals, we found that the early fluid responsible for the core of Grt1 was a relatively closed and chloride-depleted fluid system. It was close-to-neutral, with a low water–rock ratio. The core of garnet was formed by fluid diffusion in metasomatic processes. The fluid was changed into a relatively open system with reduced, chloride-rich, and weak-acid fluid. It was fluid infiltration and metasomatism that resulted in the formation of Grt1 rim and Grt2.

1 Introduction

Garnet is the most common mineral in the skarn deposit. With zonal textures, it mainly consists of grossular garnet and andradite garnet. Garnet has attracted many scholars to carry out related studies. (Jamtveit 1991; Yardley et al. 1991; Jamtveit and Andersen 1992; Jamtveit et al. 1993, 1995; Jamtveit and Hervig 1994; Smith et al. 2004; Gaspar et al. 2008; Peng et al. 2015; Park et al. 2017b; Tian et al. 2019). The method of in-situ LA–ICP–MS has been used to investigate the chemical components and structures of garnets. It has provided key information for the evolution of skarn fluid and the kinetic growth of garnet (Rakovan and Reeder 1996; Smith et al. 2004), physicochemical conditions during fluid evolution (Jamtveit et al. 1993; Zhang et al. 2017a, b; Tian et al. 2019) and fluid metasomatism (Gaspar et al. 2008).

✉ Cuihua Chen
   chencuihua@cdut.edu.cn

1 School of Earth Sciences, Chengdu University of Technology, Chengdu 610059, Sichuan, China

For many years, the Gangdese metallogenic belt of Qinghai–Tibetan plateau has been an important region in China for prospecting for ores and exploration. (Li et al. 2004; Rui et al. 2003, 2006; Hou et al. 2003a, b, 2006; Mo et al. 2003, 2005; Tang et al. 2009a, b, c, d, 2010, 2012, 2013, 2014, 2017, 2019). This belt is rich in medium to super large porphyry-skarn deposits. These polymetallic deposits are major hosts of Pb, Zn, Mo and Fe. (e.g., Mengya'a, Yaguila, Dongzhongla, Lawu, Longmala, Dongzhongsongduo, Leqingla and Xingaguo) (Tang et al. 2014). Thanks to metallogenic, geochemical and geological techniques, significant progresses have been achieved in the field of metallogenic regularity research, prospecting prediction (Hou et al. 2003b, 2006; Wang et al. 2014; Tang et al. 2012, 2014), as well as the determination of metallogenic epoch (Hou et al. 2003a; Meng et al. 2003a, b; Tang et al. 2009a, 2009b, 2009c) and ore–forming materials (Qu et al. 2002; Meng 2006, 2007; Cheng et al. 2010).

Located in northern part of southern section of Gangdese metallogenic belt, the Mengya'a lead–zinc deposit is a large skarn-type lead–zinc deposit. Skarnization is the most important alteration type in the Mengya'a area, where garnet–skarn and garnet are the main alteration results. With spatial zonation away from intrusive rock, color types of garnet vary from dark caramel, russet to pale chartreuse. Most studies have focused on the sources of ore-forming materials, using trace, rare earth elements of ores, sulfides, (Zhang 2011, 2012; Wang et al. 2012; Ye et al. 2012; Zhang et al. 2013; Lai et al. 2017) or S–Pb isotopes of sulfide (Cheng et al. 2010). Several scholars investigated the fluid evolution (Wang et al. 2011; Niu 2017) based on stable isotopes (C, O, and H) and fluid inclusions of the Mengya'a deposit. These scholars suggested that the temperature and salinity in fluids gradually decreased during early to late ore-forming stage. Ore-forming fluids were mainly derived from magmatic water with a large inflow of meteoric water. However, this theory of fluid evolution still lack mineralogical evidence (e.g., garnet) and requires further and detailed analysis on zoned garnet's structure and chemical composition. Currently, the understandings of physicochemical condition and formation of skarn fluid are still insufficient. Therefore, this paper aims to present detailed petrographic textures and in-situ LA–ICP–MS geochemical data of the Mengya'a garnet, to contribute to the theory of skarn fluid evolution and formation.

2 Regional geology

The Gangdise belt, located in Lasa terrane, has been subdivided into southern Gangdise, middle Gangdise, and northern Gangdise (Mo et al. 2003; Zhu et al. 2011). The Mengya's area is in the Pb–Zn–Ag polymetallic and metallogenic belt of the north margin of Gangdese belt (Fig. 1) (Zheng et al. 2002; Pan et al. 2006). Its regional tectonics are dominated by E–W trending structures with linear composite folds and compression–torsion thrust sheets (Cheng 2008). Regional strata include basement and cover rocks. The basement rocks mainly consist of pre–Ordovician Songduoyan group, Carboniferous-Permian Laiguzu formation, Permian Luobadui formation, Paleogene Linzizong group, and Quaternary (Niu 2017) in origin. The pre–Ordovician Songduoyan rocks are of middle–low metamorphic condition (e.g., mica-schist, slate). The Carboniferous-Permian Laiguzu formation is composed of terrigenous clastic rocks interlayered with carbonate rocks. The Permian Luobadui formation is of volcanic-bearing carbonate sedimentary construction. The Paleogene Linzizong group mainly comprises calc-alkaline and intermediate to acidic volcanic rocks.

There is a strong magmatic activity in this region, including (Fu et al. 2015): ① Late Triassic–middle Jurassic granitoid (Zhang et al. 2007), e.g., late Jurassic Xurucuo (154 Ma), Wenbu (154 Ma), Xia dingle (153 Ma) and Xiongba intrusions (149 Ma) (Zhu et al. 2008a), early cretaceous granitoid; ② Paleocene–Eocene magmatic rocks e.g., granitoid, which forms the main part of Gangdese magmatic belt; ③ Oligocene–Miocene adakite and potassic–ultra–potassic intermediate–acid magmatic rocks (Turner et al. 1996; Ji et al. 2009), which comprises monzonitic granite and biotite syenite granite. These Magmatic activities have provided conditions for the activation and modification of metallogenic materials, as well as their migration and enrichment in this region. Moreover, regional metallogenesis is related to the Oligocene–Miocene magmatic activity (Niu 2017).

3 Geology of the Mengya'a lead–zinc deposit

Mengya'a lead–zinc deposit is located in the eastern Mesozoic Island chain of Lunggar Nyainqing–Tanggula in the Gangdese–Nyainqing–Tanggula plate (Zheng et al. 2002). The main exposed strata are Late Paleozoic strata (Fig. 2), including fine clastic rocks with limestone lenses of Upper Carboniferous–Lower Permian Laigu formation, tuff and carbonate rocks in the first and second members of the Middle Permian Luobadui formation, as well as greywacke, limestone, and conglomerate of Upper Permian Lielonggou formation and Quanternary. The dominant structure is the E–W trending fault, accompanied by NE–SN trending faults. The E–W trending faults control the orebody occurrence. The main exposed magmatic rock is the quartz porphyry dike that occurs along the Laigu

formation strata. Moreover, a small amount of granite porphyry is exposed beneath the ore district.

The Mengya'a Pb–Zn deposit consists of 20 orebodies in different sizes. This study has focused on the No. Pb21 orebody, which is the second largest one, only next to No. Pb14 orebody. They are hosted by Luobadui Formation carbonate rock. This stratiform and vein-type ore deposit strikes nearly S–N and dips to the W with the angle of 54°–68°. Its main ore minerals are sphalerite and galena, with small amounts of chalcopyrite, pyrrhotite, and pyrite. Gangue minerals are mainly garnet, diopside, wollastonite, quartz, calcite with minor fluorite. The alteration of the Mengya'a deposit is dominated by skarnization, with minor silicification, carbonatation and sericitization. It is noted that chartreuse garnet is related to Pb–Zn mineralization, whereas that russet garnet is related to Fe–Cu mineralization. In the shallow part of the skarn system, garnet is widely developed in the marble contacts and occurs as fine-grained crystals of chartreuse color, accompanied by abundant Pb–Zn mineralization, which comprises the main iron orebody. In the deep part of the system towards granite porphyry, russet garnet becomes abundant and occurs as massive coarse-grained crystals with small amounts of Fe–Cu mineralization.

4 Petrographic characteristics of garnet

As the main skarn mineral, garnet is widely distributed in the area. Based on hand specimens and petrographic investigations, two generations (three types) of garnets can be distinguished. Garnets associated with Fe–Cu mineralization of the first generation (Grt1) are brown (Fig. 3a, b) and with crumble feature. Most of them have large crystals (0.1–1 cm), including pentagonal dodecahedron, rhombic dodecahedron and tetragonal triocahedron, with occurrence of chalcopyrite and pyrrhotite. Grt2 is green and characterized by fine-grained crystals with some sphalerite and galena fillings (Fig. 3c, d). In thin section, Grt1 shows euhedral and subhedral texture. It is 0.1 mm to 1 mm in size (Fig. 4a–c). The core–rim textures are well developed in garnet. The rim parts in Grt1 are optically anisotropic. Several calcite veinlets crosscut the rim sections (Fig. 4a–c). The grains of Grt2 are euhedral-subhedral and have fine-grained textures. The grains' size ranges from 0.5 to 1 mm. Like Grt1 rims, Grt2 is featured by obvious oscillatory zoning, whereas it lacks the core–rim textures (Fig. 4d–f).

5 Sampling and methods

Three representative samples, including ZK071–2, ZK071–1–1 and ZK071–1–2, were collected from the drill core. These samples were grounded into thin sections for further textural and petrographic investigation. Where garnets were recognized, more detailed petrographic examinations were undertaken, such as texture, mineral assemblage, and metasomatic replacement identifications. Representative samples were then selected for in situ major and trace element analysis. This analysis with LA-ICP-MS was carried out in Nanjing FocuMS Technology Co. Ltd. During the analysis, the laser ablation system (Photon Machines Analyte HE with 193 nm ArF Excimer) coupled to an Agilent 7700 × ICPMS was used.

Prior to LA-ICP-MS analysis, all measured points were eroded by a broad beam to eliminate potential pollutants on the surface. Helium and argon were used as the carrier gas and make–up gas, respectively. The laser was operated at 5 Hz, with a laser fluency of 6.06 J/cm^2, a spot size of 40um, and background and analysis counting times of 15 and 40 s. Element concentrations were calibrated against multiple reference materials. The preferred values of element concentrations are from the GeoReM database based on the USGS reference (http://georem.mpch-mainz.gwdg.de/). Standard reference materials CGSG–1, CGSG–2, CGSG–4, CGSG–5 and NIST SRM 612 were used for the external calibration. Detection limits were calculated for each element in each spot analysis. The off–line data processing was performed with ICPMS DataCal software (Liu et al. 2008).

6 Results

In-situ major and trace elements compositions of the Mengya'a garnets are given in Table 1. Figure 5 shows the calculated end-member compositions of garnets while the REE diagram is presented in Fig. 6.

6.1 Garnet major element geochemistry

According to major element data, both Grt1 and Grt2 are grossular–andradite (grandite) solid solution, while the compositions of other end member components, such as almandine, spessartine, pyrope and uvarovite, are < 10%.

There is a wide range of major elements components of core sections in Grt1 and Grt2 with relatively high Al contents, including Al–rich andradite (Adr_{70-98} Grs_{0-27}; Adr_{79-99} Grs_{0-19}, respectively) (Fig. 5). Grt1 rims are rich in Fe, close to nearly pure andradite (Adr_{81-100} Grs_{0-17}). We also collected data for major element compositions of

Table 1 Representative LA-ICP-MS data of two generations of garnet from the Mengya'a Pb–Zn skarn deposit

Generations of garnet	Core-Grt1											Rim-Grt1								
Spot no	ZK071-2-1	ZK071-2-2	ZK071-1-1	ZK071-1-2	ZK071-1-3	ZK071-1-2-1	ZK071-2-9	ZK071-2-5	ZK071-1-14	ZK071-1-24	ZK071-1-2-6	ZK071-2-3	ZK071-2-4	ZK071-2-6	ZK071-2-7	ZK071-2-8	ZK071-1-1-5	ZK071-1-2-2	ZK071-1-2-3	ZK071-1-2-5
SiO_2	33.0	37.5	35.7	35.5	36.3	32.8	34.6	36.6	35.7	34.6	35.5	33.5	33.2	33.7	35.9	36.7	36.3	35.1	36.4	35.0
TiO_2	2.39	0.20	1.72	3.08	4.05	3.75	1.54	0.47	0.04	0.30	0.38	0.00	0.01	0.01	0.01	0.01	0.09	0.01	0.03	0.02
Al_2O_3	2.53	1.15	3.39	3.34	4.85	4.21	2.03	0.40	0.39	3.47	2.27	0.09	0.18	0.15	0.07	0.10	0.40	0.08	0.05	0.89
FeO	22.6	28.7	23.7	23.6	21.2	22.0	27.2	31.1	29.1	24.3	26.7	31.7	33.3	30.1	29.7	31.3	29.8	31.3	29.0	28.1
MnO	0.77	1.17	0.59	0.59	0.65	0.64	0.87	0.62	1.66	0.64	0.46	0.67	0.87	0.48	0.46	0.78	0.49	0.41	0.58	0.46
MgO	0.33	0.40	0.23	0.29	0.21	0.37	0.44	0.23	0.26	0.19	0.13	0.16	0.29	0.22	0.13	0.16	0.16	0.13	0.18	0.07
CaO	37.5	29.9	33.5	32.6	31.9	35.3	32.4	29.5	31.8	35.5	33.7	32.9	31.1	34.5	32.8	30.1	31.9	32.0	32.7	34.5
Na_2O	0.00	0.01	0.02	0.01	0.01	0.00	0.01	0.03	0.00	0.01	0.00	0.00	0.00	0.00	0.00	0.00	0.00	0.00	0.00	0.00
K_2O	0.00	0.01	0.03	0.01	0.00	0.00	0.01	0.01	0.01	0.01	0.00	0.00	0.01	0.00	0.01	0.00	0.00	0.00	0.00	0.01
P_2O_5	0.01	0.01	0.00	0.00	0.00	0.02	0.00	0.00	0.02	0.01	0.00	0.00	0.00	0.00	0.00	0.00	0.00	0.00	0.00	0.00
Total	99.2	99.1	98.9	99.1	99.2	99.1	99.0	99.0	99.1	99.0	99.1	99.1	99.0	99.1	99.1	99.1	99.1	99.1	98.9	99.0
Cations on the basis of 16 oxygens																				
Si	2.76	3.13	2.97	2.94	2.97	2.73	2.91	3.09	3.02	2.89	2.97	2.87	2.86	2.87	3.03	3.10	3.05	2.99	3.06	2.95
Al iv	0.24	0.00	0.03	0.06	0.03	0.27	0.09	0.00	0.00	0.11	0.03	0.01	0.02	0.02	0.01	0.00	0.00	0.01	0.00	0.05
Al vi	0.03	0.12	0.32	0.28	0.46	0.17	0.12	0.04	0.04	0.25	0.21	0.00	0.00	0.00	0.01	0.01	0.04	0.00	0.01	0.05
Ti	0.15	0.01	0.11	0.19	0.25	0.23	0.10	0.03	0.00	0.02	0.02	0.00	0.00	0.00	0.00	0.00	0.01	0.00	0.00	0.00
Fe^{3+}	1.52	1.44	1.32	1.28	1.09	1.34	1.48	1.52	1.60	1.45	1.48	1.75	1.76	1.75	1.62	1.57	1.57	1.66	1.60	1.62
Fe^{2+}	0.06	0.57	0.33	0.36	0.36	0.19	0.43	0.68	0.46	0.25	0.39	0.52	0.65	0.40	0.48	0.65	0.53	0.57	0.45	0.36
Mn	0.05	0.08	0.04	0.04	0.04	0.05	0.06	0.04	0.12	0.05	0.03	0.05	0.06	0.03	0.03	0.06	0.03	0.03	0.04	0.03
Mg	0.04	0.05	0.04	0.04	0.03	0.05	0.05	0.03	0.03	0.02	0.02	0.02	0.04	0.03	0.02	0.02	0.02	0.02	0.02	0.01
Ni	0.00	0.00	0.00	0.00	0.00	0.00	0.00	0.00	0.00	0.00	0.00	0.00	0.00	0.00	0.00	0.00	0.00	0.00	0.00	0.00
Zn	0.00	0.00	0.00	0.00	0.00	0.00	0.00	0.00	0.00	0.00	0.00	0.00	0.00	0.00	0.00	0.00	0.00	0.00	0.00	0.00
Ca	3.36	2.68	2.98	2.90	2.80	3.15	2.92	2.67	2.88	3.18	3.02	3.02	2.87	3.15	2.96	2.72	2.88	2.91	2.95	3.12
Total	8.22	8.08	8.12	8.09	8.03	8.18	8.16	8.10	8.16	8.22	8.17	8.25	8.26	8.25	8.15	8.11	8.14	8.18	8.13	8.20
Almandine	0.00	0.00	0.00	0.00	0.00	0.00	0.00	0.00	0.00	0.00	0.00	0.00	0.00	0.00	0.00	0.00	0.00	0.00	0.00	0.00
Andradite	85.9	92.7	79.9	79.6	69.9	76.4	88.0	97.4	97.6	80.9	86.8	99.5	99.0	99.1	99.6	99.4	97.5	99.5	99.7	94.8
Grossular	10.5	1.6	17.3	17.2	27.1	20.1	7.4	0.0	0.0	16.5	11.3	0.0	0.0	0.0	0.0	0.0	0.2	0.0	0.0	3.6
Pyrope	1.53	2.15	1.13	1.50	1.09	1.73	2.17	1.21	1.31	0.86	0.63	0.52	1.05	0.88	0.42	0.63	0.83	0.50	0.30	0.35
Spessartine	2.04	3.55	1.68	1.71	1.92	1.73	2.45	1.35	1.05	1.69	1.29	0.00	0.00	0.00	0.00	0.00	1.43	0.00	0.00	1.28
Uvarovite	0.00	0.00	0.00	0.00	0.00	0.00	0.00	0.00	0.00	0.00	0.00	0.00	0.00	0.00	0.00	0.00	0.00	0.00	0.00	0.00
Trace elements (ppm) by LA-ICP-MS																				
La	1.73	16.03	0.42	1.91	1.16	2.61	9.59	1.99	20.00	1.58	0.65	2.31	5.64	2.92	14.80	5.79	1.53	1.64	3.17	1.45
Ce	5.52	13.3	1.93	6.19	4.44	8.40	14.8	2.37	18.7	4.66	3.91	0.43	2.06	0.89	6.74	2.70	1.32	0.84	3.58	6.42
Pr	1.76	2.70	0.75	2.25	1.90	3.10	3.46	0.59	4.15	1.93	1.60	0.05	0.22	0.12	0.74	0.31	0.23	0.08	0.26	1.77
Nd	10.9	14.1	6.73	15.4	15.5	23.7	18.5	3.31	18.8	13.8	10.1	0.08	0.49	0.34	1.36	0.81	1.18	0.29	0.58	7.25
Sm	4.15	3.36	3.15	5.28	7.31	7.53	5.70	1.00	2.88	5.02	2.62	0.02	0.07	0.07	0.05	0.13	0.22	0.03	0.09	1.00
Eu	0.63	0.44	0.64	0.83	0.66	1.18	2.22	0.41	0.36	1.55	0.80	0.04	0.16	0.11	0.77	0.35	0.19	0.06	1.22	0.75
Gd	5.96	3.46	5.45	7.58	12.8	11.5	7.65	1.77	3.35	9.68	3.84	0.03	0.11	0.06	0.13	0.04	0.45	0.15	0.28	0.69
Tb	1.04	0.64	0.96	1.40	2.4	2.1	1.31	0.32	0.39	1.49	0.60	0.00	0.01	0.02	0.01	0.01	0.02	0.01	0.06	0.07

Table 1 continued

Generations of garnet Spot no	Core-Grt1											Rim-Grt1								
	ZK071-2-1	ZK071-2-2	ZK071-1-1-1	ZK071-1-1-2	ZK071-1-1-3	ZK071-1-2-1	ZK071-2-9	ZK071-2-5	ZK071-1-1-4	ZK071-1-2-4	ZK071-1-2-6	ZK071-2-3	ZK071-2-4	ZK071-2-6	ZK071-2-7	ZK071-2-8	ZK071-1-1-5	ZK071-1-2-2	ZK071-1-2-3	ZK071-1-2-5
Dy	7.57	3.90	6.58	10.4	16.5	16.9	9.65	2.34	2.56	8.78	3.72	0.02	0.06	0.06	0.08	0.10	0.20	0.07	0.40	0.42
Ho	1.87	0.84	1.48	2.70	3.52	4.04	2.68	0.60	0.59	1.89	0.66	0.01	0.03	0.01	0.02	0.01	0.03	0.01	0.06	0.08
Er	5.68	2.46	4.28	8.46	8.71	11.2	7.79	1.90	1.82	5.06	1.72	0.00	0.03	0.07	0.05	0.04	0.05	0.02	0.17	0.25
Tm	0.78	0.33	0.55	1.11	1.07	1.55	1.09	0.23	0.32	0.59	0.24	0.00	0.00	0.01	0.01	0.01	0.01	0.01	0.03	0.03
Yb	5.40	2.07	3.51	6.93	5.13	10.5	6.46	1.65	1.74	3.33	1.22	0.00	0.03	0.08	0.04	0.05	0.10	0.04	0.06	0.22
Lu	0.71	0.29	0.43	1.10	0.77	1.57	1.04	0.21	0.30	0.39	0.18	0.00	0.01	0.01	0.01	0.01	0.01	0.00	0.02	0.03
Y	71.3	38.1	60.2	108	114	172	124	29.1	25.5	81.1	30.4	0.22	0.60	0.90	1.02	0.81	1.48	0.46	2.72	3.07
$\sum$REE	53.7	64.0	36.9	71.5	81.8	105.9	91.9	18.7	75.9	59.8	31.9	2.99	8.92	4.77	24.8	10.4	5.54	3.26	10.0	20.4
LREE/HREE	0.85	3.57	0.59	0.80	0.61	0.78	1.44	1.07	5.85	0.92	1.62	47.9	30.4	13.9	67.2	36.5	5.33	9.47	8.24	10.5
Eu*	0.38	0.40	0.47	0.40	0.21	0.38	1.03	0.94	0.35	0.68	0.77	5.20	5.78	5.64	28.7	14.4	1.84	2.54	22.8	2.78

Grt2

Spot no	ZK071-88-1-3	ZK071-88-1-4	ZK071-88-2-1	ZK071-88-2-2	ZK071-88-2-3	ZK071-93-1-1	ZK071-93-1-2	ZK071-93-1-3	ZK071-93-1-4	ZK071-93-2-1	ZK071-93-2-2	ZK071-93-2-3	ZK071-93-2-4
SiO_2	34.9	34.6	34.1	34.5	33.9	34.8	34.5	34.2	33.7	33.8	34.4	34.2	34.4
TiO_2	0.00	0.00	0.00	0.00	0.01	0.01	0.01	0.00	0.02	0.01	0.00	0.02	0.01
Al_2O_3	0.07	0.34	0.11	0.18	1.73	2.01	2.05	0.59	1.73	0.72	1.10	2.18	2.41
FeO	28.2	28.3	29.0	28.0	26.9	25.8	26.4	27.5	26.6	27.1	26.7	25.6	25.7
MnO	0.44	0.43	0.39	0.39	0.37	0.40	0.42	0.39	0.40	0.35	0.36	0.42	0.39
MgO	0.25	0.26	0.29	0.26	0.16	0.15	0.17	0.21	0.12	0.14	0.15	0.12	0.10
CaO	34.9	34.8	35.0	35.7	36.0	36.0	35.7	36.2	36.6	37.0	36.5	36.6	36.1
Na_2O	0.00	0.00	0.00	0.00	0.00	0.00	0.00	0.00	0.00	0.00	0.00	0.00	0.00
K_2O	0.00	0.00	0.00	0.00	0.00	0.00	0.00	0.01	0.00	0.00	0.00	0.00	0.00
P_2O_5	0.00	0.00	0.00	0.00	0.00	0.00	0.01	0.00	0.01	0.01	0.00	0.00	0.00
Total	98.8	98.8	98.9	99.0	99.1	99.2	99.2	99.1	99.2	99.2	99.2	99.2	99.2
Cations on the basis of 16 oxygens													
Si	2.96	2.94	2.90	2.92	2.86	2.92	2.90	2.89	2.84	2.86	2.90	2.88	2.89
Al iv	0.01	0.04	0.01	0.02	0.14	0.08	0.10	0.06	0.16	0.08	0.10	0.12	0.11
Al vi	0.00	0.00	0.00	0.00	0.05	0.13	0.11	0.00	0.03	0.00	0.01	0.11	0.14
Ti	0.00	0.00	0.00	0.00	0.00	0.00	0.00	0.00	0.00	0.00	0.00	0.00	0.00
Fe^{3+}	1.68	1.68	1.73	1.71	1.63	1.56	1.57	1.70	1.64	1.71	1.65	1.58	1.55
Fe^{2+}	0.32	0.33	0.33	0.28	0.28	0.25	0.28	0.25	0.23	0.21	0.23	0.22	0.25
Mn	0.03	0.03	0.03	0.03	0.03	0.03	0.03	0.03	0.03	0.03	0.03	0.03	0.03
Mg	0.03	0.03	0.04	0.03	0.02	0.02	0.02	0.03	0.01	0.02	0.02	0.02	0.01
Ni	0.00	0.00	0.00	0.00	0.00	0.00	0.00	0.00	0.00	0.00	0.00	0.00	0.00
Zn	0.00	0.00	0.00	0.00	0.00	0.00	0.00	0.00	0.00	0.00	0.00	0.00	0.00
Ca	3.17	3.16	3.19	3.24	3.25	3.23	3.21	3.28	3.31	3.36	3.29	3.29	3.25
Total	8.20	8.21	8.23	8.22	8.25	8.22	8.23	8.24	8.26	8.25	8.23	8.24	8.23

Table 1 continued

Grt2

| Spot no	ZK071-88-1-3	ZK071-88-1-4	ZK071-88-2-1	ZK071-88-2-2	ZK071-88-2-3	ZK071-93-1-1	ZK071-93-1-2	ZK071-93-1-3	ZK071-93-1-4	ZK071-93-2-1	ZK071-93-2-2	ZK071-93-2-3	ZK071-93-2-4
Almandine	0.00	0.00	0.00	0.00	0.00	0.00	0.00	0.00	0.00	0.00	0.00	0.00	0.00
Andradite	99.6	98.0	99.3	99.0	90.4	88.7	88.6	96.6	90.5	96.0	93.8	88.0	86.7
Grossular	0.0	0.0	0.0	0.0	7.8	9.5	9.5	1.3	7.9	2.4	4.5	10.3	11.8
Pyrope	0.40	1.28	0.65	1.04	0.76	0.69	0.79	1.02	0.54	0.65	0.70	0.58	0.47
Spessartine	0.00	0.70	0.00	0.00	0.99	1.07	1.11	1.06	1.04	0.95	0.98	1.11	1.04
Uvarovite	0.00	0.00	0.00	0.00	0.00	0.00	0.00	0.00	0.00	0.00	0.00	0.00	0.00
Trace elements (ppm) by LA-ICP-MS													
La	18.70	14.00	14.06	11.33	4.36	2.60	3.11	7.07	2.84	4.90	4.02	2.27	2.04
Ce	29.8	33.6	24.0	23.2	17.2	8.61	10.1	17.5	9.89	13.3	10.1	6.95	7.76
Pr	2.74	4.92	2.53	2.74	4.30	2.22	2.55	2.91	2.54	2.92	2.12	1.88	2.21
Nd	2.81	8.99	2.76	3.78	17.28	7.77	8.69	5.30	9.33	7.54	5.94	6.94	9.90
Sm	0.04	0.24	0.01	0.04	1.27	0.72	0.74	0.24	1.15	0.83	0.51	0.84	1.14
Eu	1.77	1.84	0.52	0.46	1.26	0.80	0.79	0.63	0.95	0.45	0.59	0.76	1.00
Gd	0.08	0.06	0.05	0.06	0.39	0.47	0.59	0.16	0.73	0.60	0.65	0.60	0.64
Tb	0.00	0.01	0.00	0.00	0.03	0.06	0.08	0.01	0.11	0.09	0.08	0.06	0.06
Dy	0.00	0.03	0.01	0.01	0.13	0.41	0.49	0.03	0.63	0.49	0.52	0.39	0.35
Ho	0.00	0.01	0.00	0.00	0.01	0.07	0.12	0.01	0.08	0.16	0.12	0.06	0.05
Er	0.01	0.02	0.01	0.01	0.07	0.22	0.29	0.00	0.19	0.38	0.36	0.16	0.11
Tm	0.00	0.00	0.00	0.00	0.00	0.02	0.02	0.00	0.03	0.05	0.02	0.02	0.02
Yb	0.00	0.01	0.01	0.00	0.04	0.24	0.28	0.00	0.19	0.34	0.25	0.07	0.08
Lu	0.00	0.00	0.00	0.00	0.01	0.01	0.03	0.00	0.02	0.05	0.04	0.05	0.02
Y	0.02	0.24	0.05	0.09	1.16	4.43	5.66	0.21	4.53	7.61	6.37	3.29	2.76
∑REE	55.9	63.7	44.0	41.7	46.4	24.2	27.9	33.9	28.7	32.1	25.3	21.0	25.4
LREE/HREE	682	471	503	452	66.4	15.1	13.7	160	13.6	13.9	11.4	13.9	18.2
Eu*	30.7	12.1	17.0	8.92	1.53	1.34	1.19	3.15	1.02	0.63	1.02	1.06	1.12
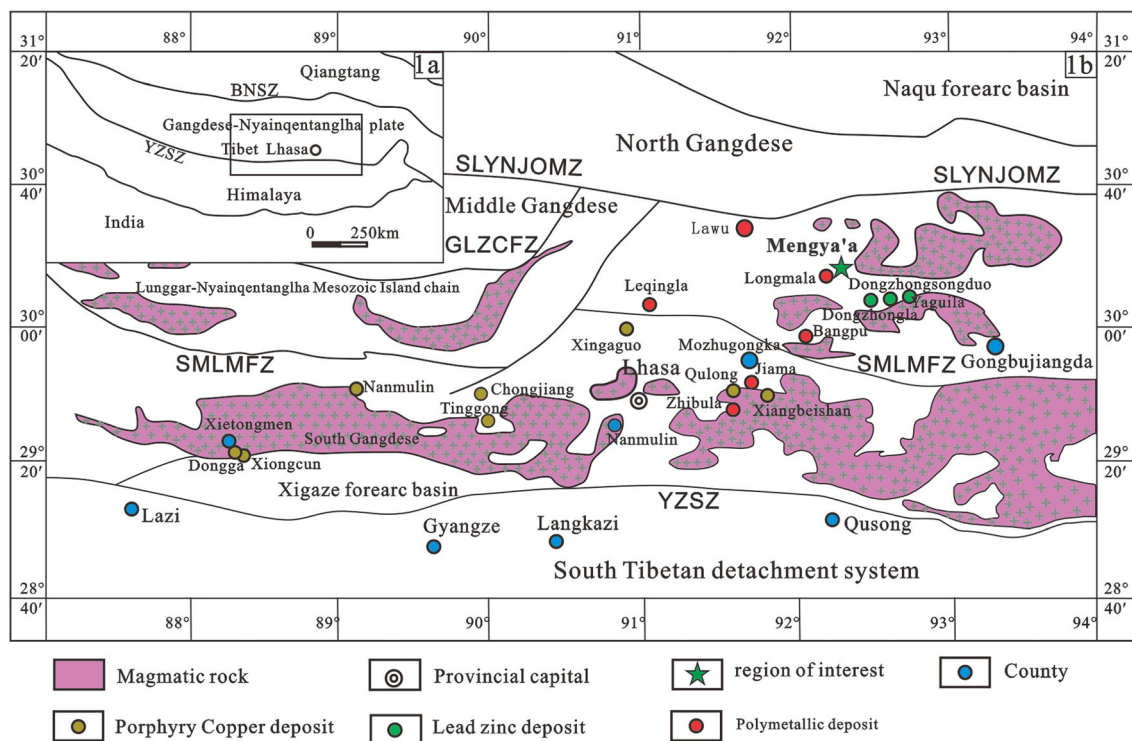
Fig. 1 Structural map of Tibet **a** geotectonic division and mineral distribution **b** in Gangdise region (modified from Cheng 2008a; Zhu et al. 2008b; Cheng et al. 2010). *BNSZ* Banggonghu-Nujiang suture zone, *YZSZ* Yarlung Tsangpo suture zone, *GLZCFZ* Ga'er-Longgeer-Zhari Namco-Cuomai fault zone, *SLYNJOMZ* Shiquanhe-Laguocuo-Yongzhu-Nam Co-Jiali ophiolite mélange zone, *SMLMFZ* Shamol-Mela-Lobadui-Mirashan fault zone

garnets in other skarn deposits, which indicates that garnets are mainly made of andradite (Fig. 5). Compared with zoned garnets from different skarn deposits worldwide (Armbruster et al. 1998; Russell et al. 1999), the Mengya'a garnets are similar to Fe–Cu skarn deposits and Pb–Zn skarn deposits (Fig. 5).

6.2 Garnet trace element geochemistry

The results indicate that these garnets are distinctively depleted in LILE (Table 1) as the radius is too large to fit in Cain the eight coordination sites of garnet. Whereas, HFSE (e.g., Zr, Hf, Nb and Ta) and REE elements in garnets are consistent to major elements and textures in the thin section. The cores from Grt1 are rich in HREE elements compared with Grt1 rims and Grt2 (Fig. 6).

Cores in Grt1 have higher total REEs ($\sum$REE = 18.7–106 ppm) (Table 1) than the rims ($\sum$REE = 3.0–24.8 ppm) and Grt2 ($\sum$REE = 21.0–65.3 ppm). In the Chondrite–normalized diagram, the cores of Grt1 have significantly rich HREEs but lack LREEs with weak negative Eu anomalies (Fig. 6a). In contrast, Grt1 rims and Grt2 exhibit rich LREE but scant HREE distribution patterns with significant positive Eu anomalies (Fig. 6).

7 Discussion

7.1 REE substitution mechanism in garnet

The chemical formula of garnet can be written as $X_3Y_2Z_3O_{12}$, where X^{2+} is Ca^{2+}, Mg^{2+}, Mn^{2+}, or Fe^{2+} in eight coordination, Y^{3+} is Fe^{3+}, Al^{3+}, or Cr^{3+} in six coordination, and Z^{4+} is Si^{4+} in a tetrahedral coordination (Deer et al. 1997). The X of having eight coordination is exclusively occupied by REEs and Y exclusively occupy X^{2+} site (Ca^{2+}). For the substitution of Eu^{2+}, instead of neutralizing electrovalence, it needs other ions to maintain electrovalence balance for REE^{3+}, U^{4+} and Y^{3+} (Shannon 1976; Smith et al. 2004). Previous studies have suggested three main substitution mechanisms (Jaffe 1951; McIntire 1963; Enami et al. 1995; Smith et al. 2004; Gaspar et al. 2008; Grew et al. 2010; Park et al. 2017a).
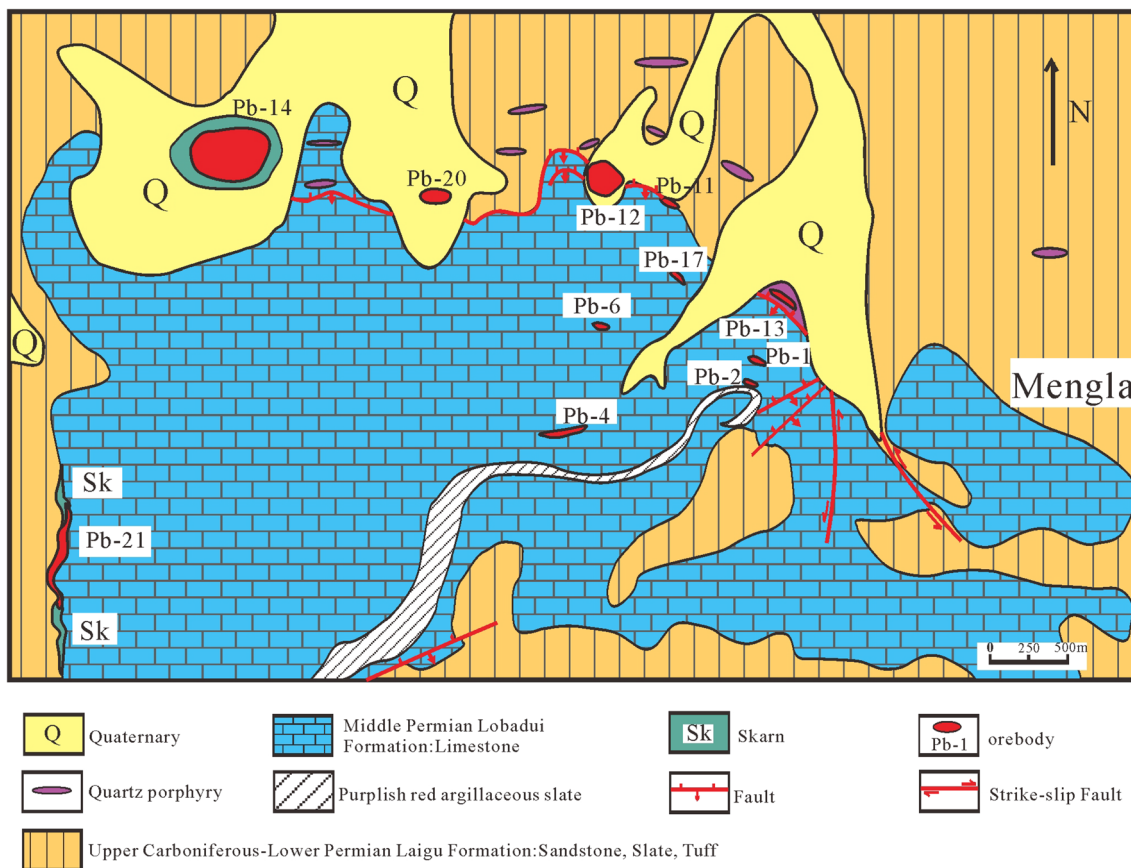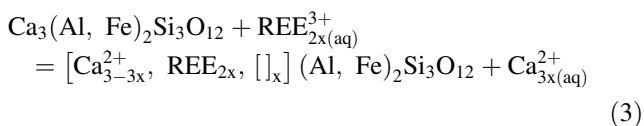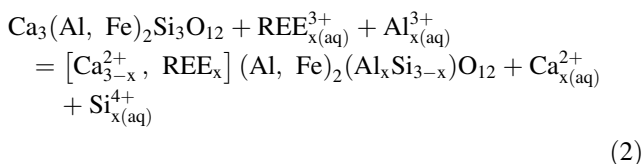
$$Ca_3(Al, Fe)_2Si_3O_{12} + REE^{3+}_{x(aq)} + Na^+_{x(aq)}$$
$$= \left[Ca^{2+}_{3-2x}, REE_x, Na_x\right](Al, Fe)_2Si_3O_{12} + Ca^{2+}_{2x(aq)}$$

(1)
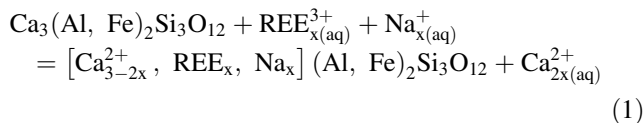
Fig. 2 Geological map of the Mengya'a ore district (modified from Cheng 2008)

$$Ca_3(Al, Fe)_2Si_3O_{12} + REE^{3+}_{x(aq)} + Al^{3+}_{x(aq)}$$
$$= \left[Ca^{2+}_{3-x}, REE_x\right](Al, Fe)_2(Al_xSi_{3-x})O_{12} + Ca^{2+}_{x(aq)}$$
$$+ Si^{4+}_{x(aq)}$$

$$(2)$$

$$Ca_3(Al, Fe)_2Si_3O_{12} + REE^{3+}_{2x(aq)}$$
$$= \left[Ca^{2+}_{3-3x}, REE_{2x}, []_x\right](Al, Fe)_2Si_3O_{12} + Ca^{2+}_{3x(aq)}$$

$$(3)$$

The Eq. (1) substitution mechanism mainly involves high Na contents in fluid (McIntire 1963; Smith et al. 2004). However, low Na concentrations (Table 1) make it difficult to detect possible correlations and evaluate the role of the Eq. (1) mechanism. Another coupled substitution of Eq. (2) is a possible substitution forming yttrium aluminum garnet (YAG) (Gaspar et al. 2008). The negative Al (IV) versus Fe^{3+} (Fig. 7a) and positive Al (IV) versus total Al (Fig. 7b) correlations, combining with the negative Al (IV) versus andradite component (Fig. 8a) and positive Al (IV) versus total REE (Fig. 8b), suggest that the incorporation of REE happens following the YAG–type substitution. Gaspar et al. (2008) pointed that Al (IV) increases with

growing Al, indicating that the garnet in an Al–rich environment would have high REE contents. REE substitution mechanism of the Mengya'a garnet suggests that the REE would preferentially concentrate in fluids in a relatively Al–rich environment when incorporating. That mechanism is distinctively different from what has formed in a Fe–rich environment (Park et al. 2017b).

7.2 Constrains of physiochemical conditions for garnet growth

7.2.1 Redox conditions of garnet formation

The relationship between Eu and the total REE content is generally different with textural types (Fig. 9a) and it verifies the variation of the fluid compositions from generation to generation. Van Westrenen et al. (2000) suggested that Eu^{2+} is lower than REE^{3+} in terms of the relaxation energy required for entering Ca sites, but it is higher than Eu^{3+} for D garnet/fluid REE between grandite garnet and aqueous fluids (Smith et al. 2004). Furthermore, Eu^{2+} makes of a predominant share in skarn systems above

Fig. 3 Hand specimen characteristic of brown and green garnets collected from drill holes in the Mengya'a deposit. **a**, **b** Massive brown granular garnet (Grt1) replaced by quartz. **c**, **d** Massive granular green garnet (Grt2) replaced by quartz. *Grt* Garnet, *Q* Quartz
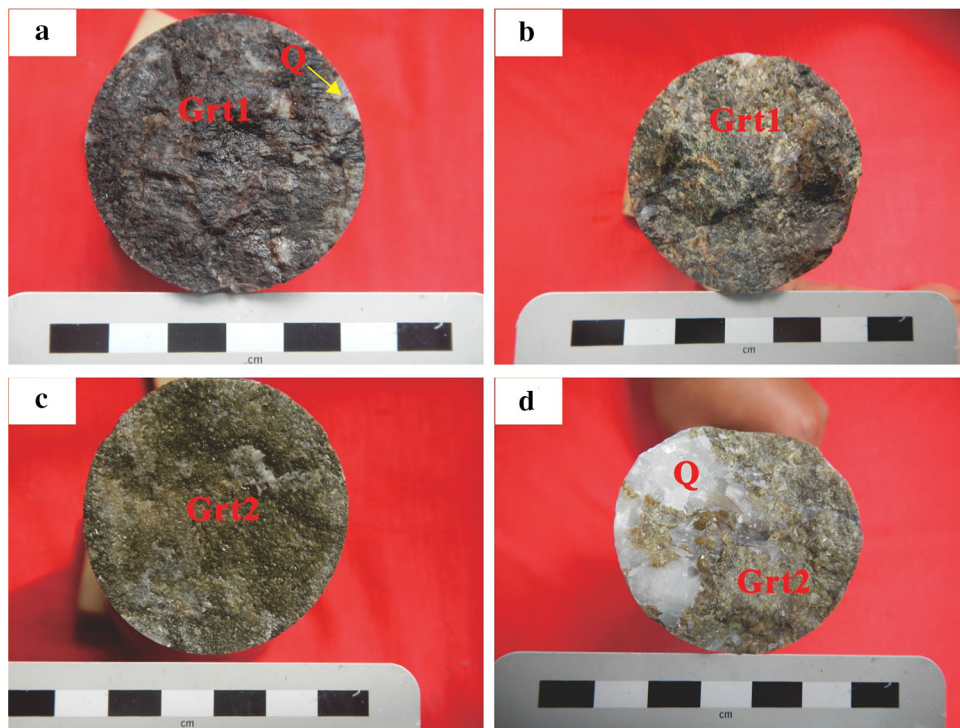
250 °C (Bau 1991; Sverjensky 1984), where the stability of soluble Eu^{2+} is enhanced by chlorine (Mayanovic et al. 2002, 2007), while the partitioning of Eu depends on the oxygen fugacity of the fluid (fO_2) (Allen and Seyfried, 2005). Thus, the positive shift in the europium anomaly is probably caused by the rich divalent europium in the residual fluid (i.e., the infiltration fluid). The Eu in the Grt1 rims and Grt2 is positively fractionated, compared with other REEs (Fig. 6), showing a reduced- and Cl-enriched system. In contrast, the negative Eu anomaly characterized most of the Grt1 cores (Fig. 6a) which are likely originated from an Eu-depleted fluid source or from a Cl-depleted system.

7.2.2 pH condition of garnet formation

For factors that control water–rock interaction, pH significantly affects REE fractionation in skarn hydrothermal fluids, so hydrothermal fluids are featured with distinctive REE patterns (Bau 1991). When the pH is close-to-neutral, hydrothermal fluids are HREE-enriched and LREE-depleted with negative or no Eu anomaly. When the conditions are mild acid, the REE patterns are relatively LREE-enriched but HREE-depleted with distinct positive Eu anomalies (Bau, 1991; Allen and Seyfried, 2005; Gaspar et al. 2008; Mayanovic et al. 2002, 2007). REE patterns and Eu anomalies reflect pH conditions of hydrothermal fluids (Sverjensky 1984; Bau 1991; Van Westrenen et al.

2000; Smith et al. 2004; Allen and Seyfried 2005; Park et al. 2017b). This method has been widely used to constrain conditions that facilitate garnet formation (Zhai et al. 2014; Zhang et al. 2017a, 2017b; Xiao et al. 2018; Tian et al. 2019).

The distinctive REE patterns and Eu anomalies in Mengya'a garnet record the variation of fluid pH condition. The Grt1 core sections exhibit a clear pattern of rich HREE and depleted LREE with negative Eu anomalies (Fig. 6a), suggesting that the fluid that forms core sections is close to neutral. In comparison, the downward-sloping (LREE-enriched and HREE-depleted) trend with positive Eu anomalies in Grt1 rims and Grt2 indicates that they were made of mild-acid fluid. Furthermore, due to the Cl^--enriched fluid under weak acidic condition (Bau 1991), the acidic fluid can transport Eu in EuCl2- 4complex (Allen and Seyfried 2005) and form positive Eu anomalies based on increasingly stable Eu^{2+} (Mayanovic et al. 2002, 2007; Gaspar et al. 2008). Such mechanism might lead to LREE–enriched and HREE–depleted patterns and positive Eu anomalies in Grt1 rims and Grt2 (Fig. 6).

7.3 The formation of garnet

Skarn forms through a dynamic process, involving several hydrothermal stages and a constant fluid evolution process (Meinert 1982; Meinert et al. 2005). Skarn zonation is usually consistent with the predictions of metasomatic

Fig. 4 Petrographic images showing textural features of garnets from Mengya'a deposit. **a–c** Core–rim textures are widely developed in Grt1 and the rims show oscillatory zones. It is noted that some epidote replaced core sections and some calcite veinlets replace rims along oscillatory zones. **d–f** The fine-grained Grt2 is optically isotropic feature without core–rim textures which replaced by calcite. *Cal* Calcite, *Ep* Epidote
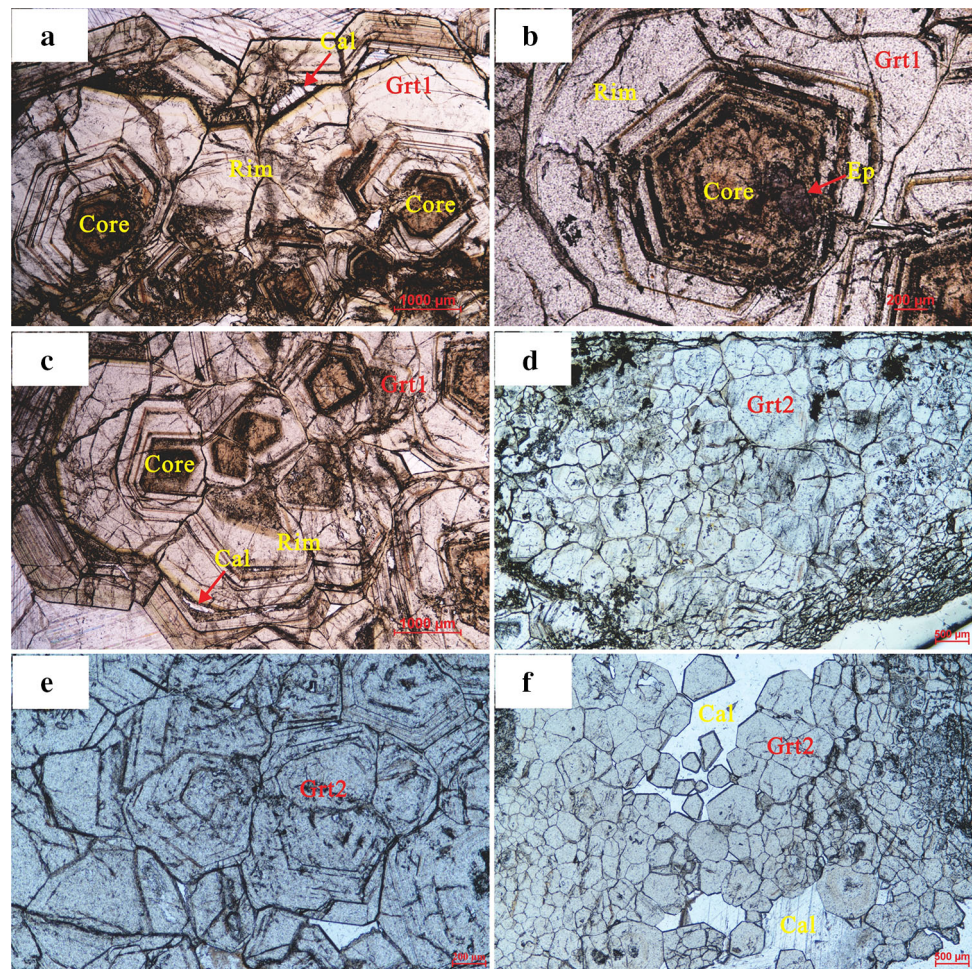
zoning theory (Korzhinskii 1968), reflecting fluid dynamics changes (diffusion or infiltration) (Gaspar et al. 2008). Our study delves into the formation of garnet, exploring the structure from core to rim and tracking its influence on the composition of garnet.

Hydrothermal fluid metasomatism is subject to the skarn system, which includes a closed system for diffusive metasomatism and an open system for infiltrative metasomatism (Gaspar et al. 2008; Park et al. 2017b). The correlation between Y and REE^{3+} (Park et al. 2017b) might reflect and identify properties of the system. If REE and Y show an apparent linear correlation, it is indicative of a closed system, otherwise, there could be an open system (Park et al. 2017b). Furthermore, previous studies suggested that the andradite with LREE-enriched patterns shows no linear relationship between REE and Y, indicating that this type of garnets are crystallized at disequilibrium in an open system through infiltrative metasomatism. The Al–rich andradite with HREE-enriched patterns has a significant linear relationship between REE and Y, indicating its crystallization took place at

equilibrium in the closed system through diffusion metasomatism. In this study, the Grt1 cores and rims show a linear correlation between total REEs and Y (Fig. 9b), indicating that such texture is crystallized in equilibrium or under a stagnant state. However, the Grt1 rims exhibit andradite components with apparent REE patterns and LREE-enriched, HREE-depleted patterns (Fig. 6a). Therefore, geochemical signature of Grt1 rims cannot explain the distinguished REE patterns between core and rim sections. Compared to Grt1, the Grt2 is characterized by the absence of a correlation between Y and the total REEs, which can be explained by infiltration metasomatism.

In addition, the garnet studied in this paper shows distinctive textures, indicating their different kinetics of growth. In skarn environments, fluid infiltration is pervasive because of extensively brittle deformation (Einaudi et al., 1981; Meinert, 1992; Ciobanu and Cook, 2004), which leads to microfractures hosting the Grt1 rims and Grt2 (Fig. 4). When pressure is released under an open system, this textural type could be strongly influenced by
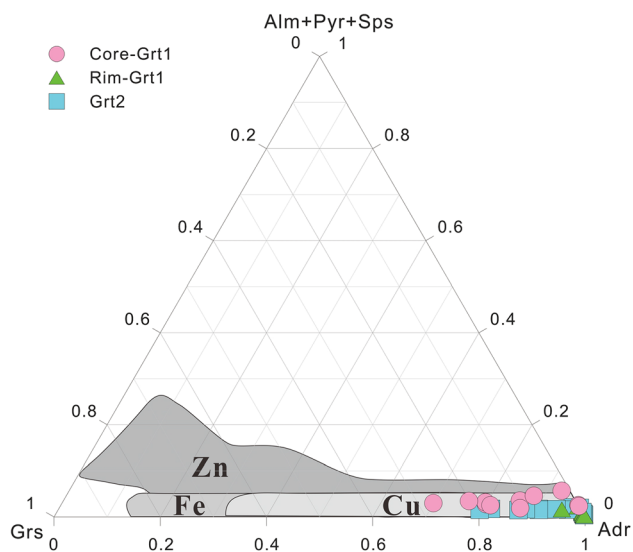
Fig. 5 Classification of garnet in the Mengya'a Pb–Zn skarn deposit, comparing to the garnet from Fe, Cu, and Zn skarn deposits worldwide (modified after Meinert 1992). *Sps* spessartine, *Pyr* Pyrope, *Alm* almandine, *Grs* grossular, *Adr* andradite

infiltration metasomatism. The fluid inclusions and rapidly grown textures (e.g., trapezohedral {211} crystal faces) of Gr1 rims and Grt2 also support the crystallization through infiltration metasomatism at high water/rock (W/R) ratios. By contrast to Grt1 rims and Grt2, the Grt1 cores lack fluid inclusions, microfractures, and rapidly grown textures (Fig. 4), representing the fact that garnet cores grow slowly under diffusive metasomatism at low W/R ratios. These features are considered to reflect periodic fluid fluctuation, showing that Grt1 cores crystallizes in a closed system

through diffusive metasomatism, while Grt1 rims and Grt2 forms in an open system by infiltrative metasomatism.

8 Conclusions

The Mengya'a Pb–Zn deposit is a large skarn deposit in the east section of Gangdese metallogenic belt. Garnet is the deposit's predominant mineral with a widely developed oscillatory zonation. According to our study on texture and chemical composition of garnet, this paper draws following conclusions:

(1) According to on hand specimen and optical characteristics, there are two generations of garnets identified in the Mengya'a deposit. Garnets of the first generation (Grt1) associated with Fe–Cu mineralization are coarse-grained brown crystals with core–rim textures in oscillatory zoning, while garnets of the second generation (Grt2) associated with Pb–Zn mineralization are fine-grained green crystals with oscillatory zonings. In addition, Mengya'a garnets are mainly made up of andradite as one of the grossular–andradite solid solution series.

(2) The incorporation of REEs into the Grt1 and Grt2 is likely dependent on the substitution mechanism of $[X^{2+}]^{VIII}$ $_{-1}[REE^{3+}]^{VIII}$ $_{+1}[Si^{4+}]^{IV}$ $_{-1}[Z^{3+}]^{IV}$ $_{+1}$ in the Al-enriched environment. The Grt1 cores with HREE-enriched patterns and weak negative Eu anomalies are crystallized from Cl-depleted close-to-neutral fluids, whereas the Grt1 rims and Grt2 with LREE-enriched patterns and positive Eu
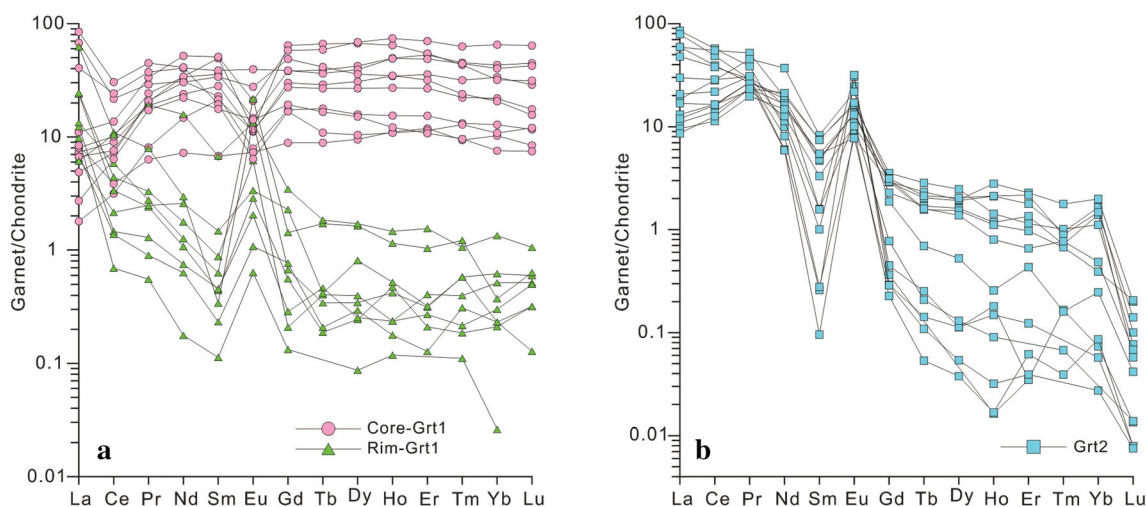

Fig. 6 Chondrite-normalized REE patterns for two generations of Mengya'a garnets. The chondrite-normalized values were calculated by McDonough and Sun (1995)
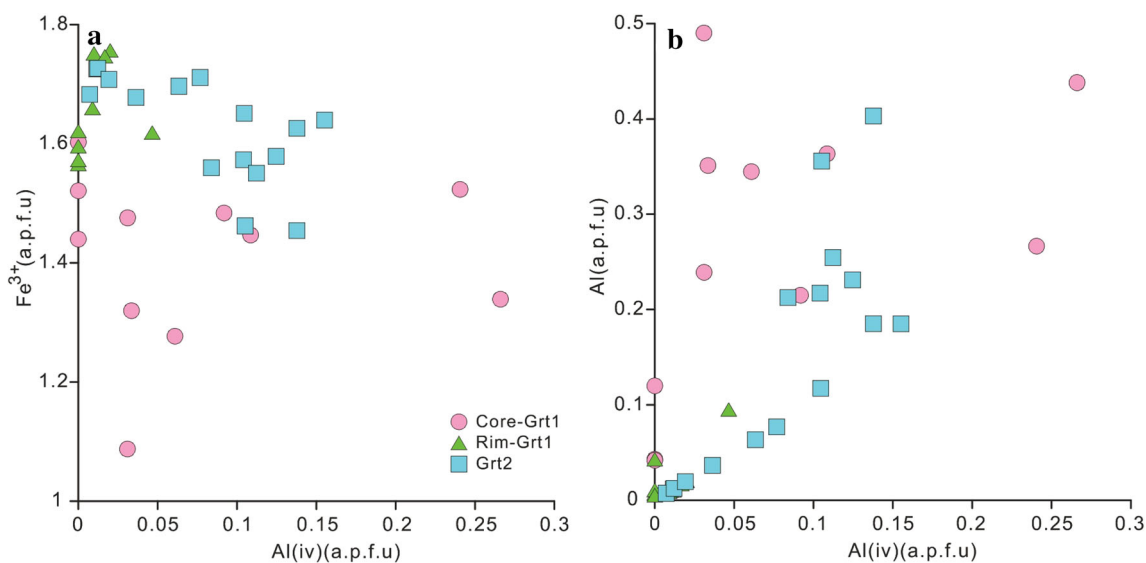
Fig. 7 Scatter diagrams of tetrahedral Al (IV) against **a** Fe^{3+} and **b** Al. Data in atoms per formula unit (apfu)
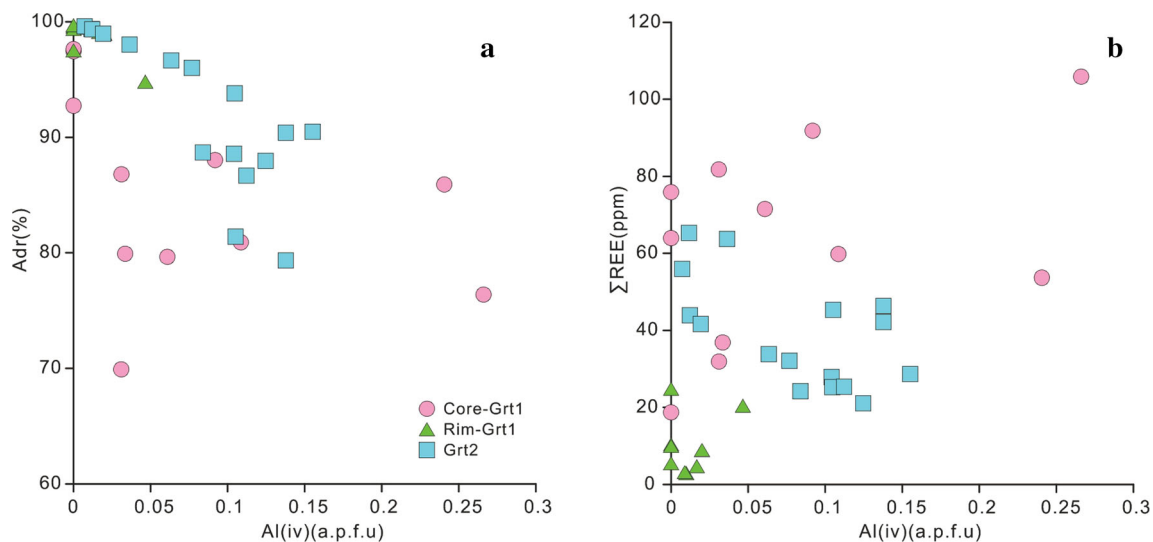

Fig. 8 Variation of tetrahedral Al (IV) with andradite composition and total REEs in garnets from Mengya'a: **a** tetrahedral Al (IV) in apfu versus percentage of andradite end-member component in garnet including information on their texture character; **b** tetrahedral Al (IV) in apfu versus total REEs

anomalies are crystallized in a reduced, Cl-enriched weak-acidic fluids.

(3) The early skarn fluid is a relatively closed system with low water/rock ratio and mainly in diffusive metasomatism, facilitating the formation of Grt1 cores with Al–enriched andradite. In comparison, the late skarn fluid is an open system with high water/rock ratio and infiltrative metasomatism, resulting in
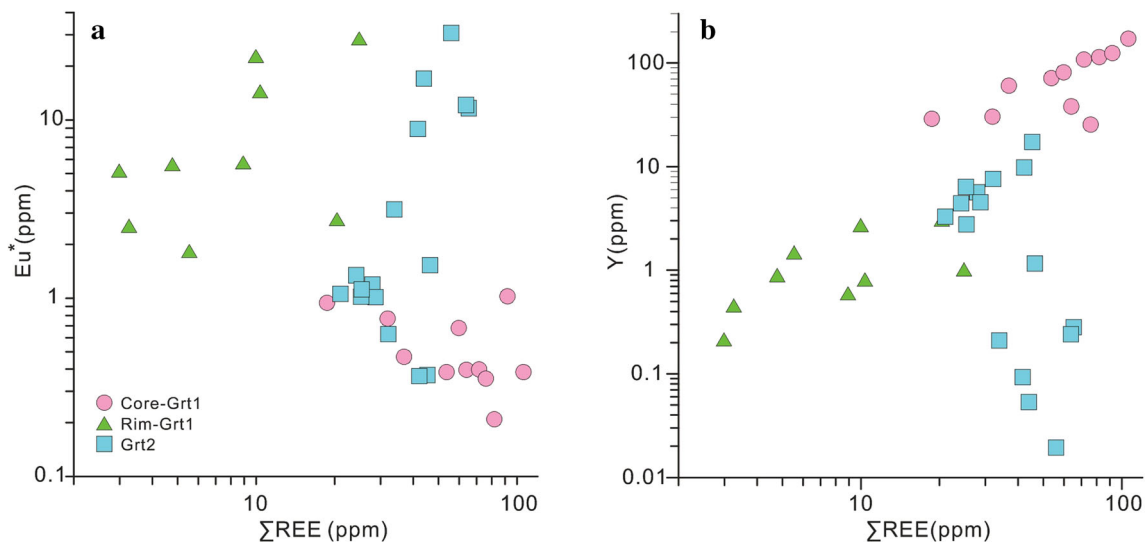
Fig. 9 Plots of Eu* versus ΣREE **a** and ΣREE versus Y **b** of in garnets from the Mengya'a deposit

the formation of Grt1 rims and Grt2 with oscillatory zone.

References

Allen DE, Seyfried WE Jr (2005) REE controls in ultramafic hosted MOR hydrothermal systems: an experimental study at elevated temperature and pressure. Geochim Cosmochim Acta 69:675–683

Armbruster T, Birrer J, Libowitzky E, Beran A (1998) Crystal chemistry of Ti-bearing andradites. Eur J Mineral 10:907–921

Bau M (1991) Rare–earth element mobility during hydrothermal and metamorphic fluid rock interaction and the significance of the oxidation state of europium. Chem Geol 93:219–230

Cheng SB (2008) Geological characteristics and genesis of Mengya'a layered skarn Lead-Zinc Deposit in Tibet. Dissertation, Wuhan: China University of Geosciences (**in Chinese with English abstract**)

Cheng SB, Pang YC, Cao L (2008) The genesis of mengya'a skarn-type lead-zinc deposit, Tibet. Geol Miner Resour South China 3:50–56 (**in Chinese with English abstract**)

Cheng WB, Gu XX, Tang JX, Wang LQ, Lv PR, Zhong KH, Liu XJ, Gao YM (2010) Lead isotope characteristics of ore sulfides from typical deposits in the Gangdise Nianqing Tanggula metallogenic belt, Tibet: implications for the zonation of ore forming elements. Acta Petrologica Sinica 26:3350–3362 (**in Chinese with English abstract**)

Ciobanu CL, Cook NJ (2004) Skarn textures and a case study: the Ocna de Fier-Dognecea orefield, Banat, Romania Science Direct. Ore Geol Rev 24:315–370

Deer WA, Howie RA, Wise WS, Zussman J (1997) Rock-forming minerals. Framework Silicates: Silica Minerals, Feldspathoids and the Zeolites. Geological Society of London.

Einaudi MT, Meinert LD, Newberry RJ (1981) Skarn deposits. Economic Geology Seventy Fifth Anniversary Volume:317–391

Enami M, Bolin C, Yoshida T, Kawabe I (1995) A mechanism for Na incorporation in garnet: an example from garnet in orthogneiss from the Su-Lu terrane, eastern China. Am Mineral 80:475–482

Fu Q, Huang KX, Zheng YC, Yang ZS, Duan LF (2015) Ar-Ar age of muscovite from skarn orebody of the Mengya'a lead-zinc deposit in tibet and its geodynamic significance. Acta Geol Sin 89:569–582 (**in Chinese with English abstract**)

Gaspar M, Knaack C, Meinert LD, Moretti R (2008) REE in skarn systems: a LA–ICP–MS study of garnets from the crown jewel gold deposit. Geochim Cosmochim Acta 72:185–205

Grew ES, Marsh JH, Yates MG, Lazic B, Armbruster T, Locock A, Bell S W, Dyar M D, Bernhardt H J and Medenbach O (2010) Menzerite-(Y), a new species, $\{(Y, REE)(Ca, Fe^{2+})_2\}[(Mg, Fe^{2+}) (Fe^{3+}, Al)] (Si_3) O_{12}$, from a felsic granulite, Parry Sound, Ontario, and a new garnet end-member, $\{Y_2Ca\}[Mg_2](Si_3)O_{12}$. Can Mineral 48:727–749

Hou ZQ, Qu XM, Wang SX, Gao YF, Du AD, Huang W (2003a) Re-Os age of Molybdenite in the Gangdise porphyry copper belt, Tibet Plateau: metallogenic time limit and dynamic background application. Sci China (Series D) 33:609–618 (**in Chinese with English abstract**)

Hou ZQ, Lv QT, Wang AJ, Li XB, Wang ZQ, Wang EQ (2003b) Continental collision and related metallogeny: a case study of mineralization in Tibetan Orogen. Miner Depos 22:319–333 (**in Chinese with English abstract**)

Hou ZQ, Mo XX, Yang ZM, Wang AJ, Pan GT, Qu XM, Nie FJ (2006) Metallogeneses in the collisional orogen of the Qinghai-Tibet Plateau: Tectonic setting, tempo-spatial distribution and ore deposit types. Geol China 33:348–359 (**in Chinese with English abstract**)

Jaffe HW (1951) The role of yttrium and other minor elements in the garnet group. Am Miner 36:133–155

Jamtveit B (1991) Oscillatory zonation patterns in hydrothermal grossular–andradite garnet; nonlinear dynamics in regions of immiscibility. Am Miner 76:1319–1327

Jamtveit B, Andersen TB (1992) Morphological instabilities during rapid growth of metamorphic garnets. Phys Chem Miner 19:176–184

Jamtveit B, Wogelius RA, Fraser D (1993) Zonation patterns of skarn garnets: records of hydrothermal system evolution. Geology 21:113–116

Jamtveit B, Hervig RL (1994) Constraints on transport and kinetics in hydrothermal systems from zoned garnet crystals. Science 263:505–508

Jamtveit B, Ragnarsdottir KV, Wood BJ (1995) On the origin of zoned grossular–andradite garnets in hydrothermal systems. Eur J Miner 7:1399–1410

Ji WQ, Wu FY, Zhong SL, Liu CZ (2009) Geochronology and petrogenesis of granitic rocks in Gangdese batholith, southern Tibet. Sci China Ser D-Earth Sci 39:849–871 (**in Chinese with English abstract**)

Korzhinskii DS (1968) The theory of metasomatic zoning. Miner Deposita 3:222–231

Lai X, Chen CH, Tu ZL, Zhang Y, Song ZJ, Gu Y, Chen XJ, Yang DP (2017) Geochemical characteristics of skarn rocks of the Mengya'a Pb-Zn deposit in Tibet. Miner Resour Geol 31:1063–1071 (**in Chinese with English abstract**)

Li GM, Pan GT, Wang GM, Huang ZY, Gao DF (2004) Prospect evaluation and prospect of mineral resources in Gangdise metallogenic belt Tibet. J Chengdu Univ Technol 31:22–27 (**in Chinese with English abstract**)

Liu YS, Hu ZC, Gao S, Günther D, Xu J, Gao CG, Chen HH (2008) In situ analysis of major and trace elements of anhydrous minerals by LA–ICP–MS without applying an internal standard. Chem Geol 257:34–43

Mayanovic RA, Jayanetti S, Anderson AJ, Bassett WA, Chou IM (2002) The structure of Yb^{3+} aquaion and chloro complexes in aqueous solutions at up to 500 °C and 270 MPa. J Phys Chem A 106:6591–6599

Mayanovic RA, Anderson AJ, Bassett WA, Chou IM (2007) On the formation and structure of rare–earth element complexes in aqueous solutions under hydrothermal conditions with new data on gadolinium aqua and chloro complexes. Chem Geol 239:266–283

McDonough WF, Sun SS (1995) The composition of the Earth. Chem Geol 120:223–253

McIntire W (1963) Trace element partition coefficients–areview of theory and applications to geology. Geochim Cosmochim Acta 27:1209–1264

Meinert LD (1982) Skarn, manto, and breccia pipe formation in sedimentary rocks of the Cananea mining district, Sonora, Mexico. Econ Geol 77:919–949

Meinert LD (1992) Skarns and skarn deposits. Geosci Can 19:145–162

Meinert L, Dipple G, Nicolescu S (2005) World skarn deposits. Economic Geology 100th Anniversary Volume: 299–336

Meng XJ, Hou ZQ, Gao YF, Huang W, Qu XM, Qu WJ (2003a) Development of porphyry copper-molybdenum-lead-zinc ore-_forming system in east Gangdese Belt, Tibet: evidence from Re-Os age of molybdenite in Bangpu copper polymetallic deposit. Miner Depos 22:246–252 (**in Chinese with English abstract**)

Meng XJ, Hou ZQ, Gao YF, Huang W, Qu XM, Qu WJ (2003b) Re-Os dating for molybdenite from Qulong porphyry copper deposit in Gangdese metallogenic belt, Xizang and its metallogenic significance. Geol Rev 49:660–666 (**in Chinese with English abstract**)

Meng XJ, Hou ZQ, Li ZQ (2006) Sulfur and lead isotope compositions of the Qulong porphyry copper deposit, Tibet: implications for the sources of plutons and metals in the deposit. Acta Geol Sinica 80:554–560 (**in Chinese with English abstract**)

Meng XJ, Hou ZQ, Ye PS, Yang ZS, Li ZQ, Gao YF (2007) Characteristics and ore potentiality of Gangdese silver-poly-metallic mineralization belt in Tibet. Depos Geol 26:153–162 (**in Chinese with English abstract**)

Mo XX, Zhao ZD, Deng JF, Dong GC, Zhou S, Guo TY, Zhang SQ, Wang LL (2003) Response of volcanism to the India-Asia collision. Earth Sci Front 10:135–148 (**in Chinese with English abstract**)

Mo XX, Dong GC, Zhao ZD, Zhou S, Wang LL, Qiu RZ, Zhang FQ (2005) Spatial and Tamporal distribution and characteristics of granitoids in the Gangdes, Tibet and implication for crustal growth and evolution. Geol J China Univ 11:281–290 (**in Chinese with English abstract**)

Niu YT (2017) Characteristics of fluid inclusions and its significance in Mengya'a Pb-Zn deposit, Tibet. Master's thesis, Chengdu University of Technology (**in Chinese with English abstract**)

Pan GT, Mo XX, Hou ZQ, Zhu DC, Wang LQ, Li GM, Zhao ZD, Geng QR, Liao ZL (2006) Spatial-temporal framework of the Gangdese orogenic belt and its evolution. Acta Petrol Sinica 22:521–533 (**in Chinese with English abstract**)

Peng HJ, Zhang CQ, Mao JW, Santosh M, Zhou YM, Hou L (2015) Garnets in porphyry–skarn systems: a LA–ICP–MS, fluid inclusion, and stable isotope study of garnets from the Hong-niu-Hongshan copper deposit, Zhongdian area, NW Yunnan Province, China. J Asian Earth Sci 103:229–251

Park C, Choi W, Kim H, Park M, Kang I, Lee H, Song Y (2017a) Oscillatory zoning in skarn garnet: implications for tungsten ore exploration. Ore Geol Rev 89:1006–1018

Park C, Song Y, Kang I, Shim J, Chung D, Park C (2017b) Metasomatic changes during periodic fluid flux recorded in grandite garnet from the Weondong W–skarn deposit, South Korea. Chem Geol 451:135–153

Qu XM, Hou ZQ, Li YG (2002) Implications of S and Pb isotopic compositions of the material Gangdise porphyry copper belt for the ore-forming source and material recycling within the orogenicng belt. Geol Bull China 21:768–776 (**in Chinese with English abstract**)

Rakovan J, Reeder RJ (1996) Intracrystalline rare earth element distributions in apatite: Surface structural influences on incorporation during growth. Geochim Cosmochim Acta 60:4435–4445

Rui ZY, Hou ZQ, Qu XM, Zhang LS, Wang LS, Liu YL (2003) Metallogenetic epoch of Gangdese porphyry copper belt and uplift of Qinghai-Tibet Plateau. Miner Depos 22:217–225 (**in Chinese with English abstract**)

Rui ZY, Hou ZQ, Li GM, Liu B, Zhang LS, Wang LS (2006) A genetic model for the gandis porphyry copper deposits. Geol Rev 52:459–466 (**in Chinese with English abstract**)

Russell JK, Dipple GM, Lang JR, Lueck B (1999) Major-element discrimination of titanian andradite from magmatic and hydrothermal environments: an example from the Canadian Cordillera. Eur J Miner 11:919–935

Shannon RD (1976) Revised effective ionic radii and systematic studies of interatomic distances in halides and chalcogenides. Acta Crystallogr A32:751–767

Sverjensky DA (1984) Europium redox equilibria in aqueous solution. Earth Planet Sci Lett 67:70–78

Smith M, Henderson P, Jeffries T, Long J, Williams C (2004) The rare earth elements and uranium in garnets from the Beinn an Dubhaich Aureole, Skye, Scotland, UK: constraints on processes in a dynamic hydrothermal system. J Petrol 45(3):457–484

Tang JX, Chen YC, Wang DH, Wang CH, Xu YP, Qu WJ, Huang Y (2009a) Dating of molybdenite from the Sharang porphyry

molybdenum deposit in Gongbo'gyamda County, Tibet and its geological significance. Acta Geol Sin 83:698–704 (**in Chinese with English abstract**)

Tang JX, Wang CH, Qu WJ, Du AD, Ying LJ, Gao YM (2009b) Re-Os isotopic dating of molybdenite from the Yulong porphyry copper-molybdenum deposit in Tibet and its metallogenic significance. Rock Miner Anal 28:215–218 (**in Chinese with English abstract**)

Tang JX, Chen YC, Duo J, Liu HF, Gao YM (2009c) The main deposit types, ore-forming regularity and the prospecting evaluation of the eastern Gangdese metallogenic belt. Acta Miner Sinica 29:476–478 (**in Chinese with English abstract**)

Tang JX, Zhang L, Huang Y, Wang CH, Li ZJ, Deng Q, Wang Y (2009d) 40Ar/39Ar isotope ages of main geological bodies in Xiongcun copper-gold deposit, Xietongmen County, Tibet, and their geological significance. Miner Depos 28:759–769 (**in Chinese with English abstract**)

Tang JX, Wang DH, Wang XW, Zhong KH, Ying LJ, Zheng WB, Li FJ, Guo N, Qin ZP, Yao XF, Li L, Wang Y, Tang XQ (2010) Geological features and metallogenic model of the Jiama copper-polymetallic deposit in Tibet. Acta Geoscientica Sinica 31:495–506 (**in Chinese with English abstract**)

Tang JX, Duo J, Liu HF, Lang XH, Zhang JS, Zheng WB, Ying LJ (2012) Minerogenetic series of ore deposits in the east part of the Gangdise metallogenic belt. Acta Geoscientica Sinica 33:393–410 (**in Chinese with English abstract**)

Tang JX, Zhang Z, Li ZJ, Sun Y, Yao XF, Hu ZH, Wang HX, Song JL, He L (2013) The Metallogensis, deposit model and prospecting direction of the Ga'erqiong-Galale copper-gold ore field, Tibet. Acta Geoscientica Sinica 34:385–394 (**in Chinese with English abstract**)

Tang JX, Wang LQ, Zheng WB, Zhong KH (2014) Ore deposits metallogenic regularity and prospecting in the eastern section of the Gangdese metallogenic belt. Acta Geol Sin 88:2545–2555 (**in Chinese with English abstract**)

Tang JX, Wang Q, Yang HH, Gao X, Zhang ZB, Zou B (2017) Mineralization, exploration and resource potential of porphyry-skarn-epithermal copper polymetallic deposits in Tibet. Acta Geoscientica Sinica 38:571–613 (**in Chinese with English abstract**)

Tang JX (2019) Mineral resources base investigation and research status of the Tibet Plateau and its adjacent major metallogenic belts. Acta Petrologica Sinica 35:617–624 (**in Chinese with English abstract**)

Tian ZD, Leng CB, Zhang XC, Zafar T, Zhang LJ, Hong W, Lai CK (2019) Chemical composition, genesis and exploration implication of garnet from the Hongshan Cu–Mo skarn deposit. SW China Ore Geol Rev 112:103016

Turner S, Hawkesworth C, Calsteren PV, Heath E, Macdonald R, Black S (1996) U-series isotopes and destructiveplate margin magma genesis in the Lesser Antilles. Earth Planet Sci Lett 142:191–207

Van Westrenen W, Allan N, Blundy J, Purton J, Wood B (2000) Atomistic simulation of trace element incorporation into garnets–comparison with experimental garnet–melt partitioning data. Geochim Cosmochim Acta 64:1629–1639

Wang LQ, Gu XX, Tang JX, Wang H, Xiang HY (2011) Source and characteristics of ore-forming fluids in the Mengya'a Pb–Zn deposit, Tibet. J Chengdu Univ Technol 38:67–75 (**in Chinese with English abstract**)

Wang LQ, Cheng WB, Luo MC, Xiang HY (2012) A study of metallic sulfides, quartz REE composition characteristics and genesis of the Mengya'a lead–zinc deposit. Geol China 39:740–749 (**in Chinese with English abstract**)

Wang LQ, Lin X, Li Z, Zhang Z, Kang HR, Li HF (2014) Geochronology, geochemistry and Hf isotopic compositions of

the granite porphyry in the Mengya'a Pb-Zn deposit, Tibet. Acta Geol Sinica 88:2572–2583 (**in Chinese with English abstract**)

Xiao X, Zhou TF, White NC, Zhang LJ, Fan Y, Wang FY, Chen XF (2018) The formation and trace elements of garnet in the skarn zone from the Xinqiao Cu–S–Fe–Au deposit, Tongling ore district, Anhui Province, Eastern China. Lithos 302:467–479

Yardley B, Rochelle C, Barnicoat A, Lloyd G (1991) Oscillatory zoning in metamorphic minerals: an indicator of infiltration metasomatism. Mineral Mag 55:357–365

Ye YQ, Li ZQ, Ni SJ, Zhang ZZ (2012) Elemental Geochemical Characteristics of Mengya'a skarn Lead-Zinc Deposit in Tibet. West-China Explor Eng 12:99–103 (**in Chinese with English abstract**)

Zhang HF, Xu WC, Guo JQ, Zong KQ, Cai HM, Yuan HL (2007) Zircon U-Pb and Hf isotopic composition of deformed granite in the southern margin of the Gangdese belt, Tibet: evidence for early Jurassic subduction of Neo-Tethyan oceanic slab. Acta Petrologica Sinica 23:1347–1353 (**in Chinese with English abstract**)

Zhang Y, Liu QQ, Shao YJ, Li HB (2017a) Fingerprinting the hydrothermal fluid characteristics from LA–ICP–MS trace element geochemistry of garnet in the Yongping Cu deposit, SE China. Minerals 7:199–226

Zhang Y, Shao YJ, Wu CD, Chen HY (2017b) LA–ICP–MS trace element geochemistry of garnets: Constraints on hydrothermal fluid evolution and genesis of the Xinqiao Cu–S–Fe–Au deposit, eastern China. Ore Geol Rev 86:426–439

Zhang ZZ (2011) Geology, geochemistry and origin of ore-forming substances of Mengya'a skarn lead and zinc ore deposit, Tibet, China. Dissertation, Chengdu University of Technology (**in Chinese with English abstract**)

Zhang ZZ, Li ZQ, Chen SB, Wang JZ, Ye YQ, Xiao H (2012) Geochemical characteristics of granite porphyry of Mengya'a skarn Pb-Zn deposit in Tibet. Nonferrous Metals 64(5):49–54 (**in Chinese with English abstract**)

Zhang ZZ, Li ZQ, Wang JQ, Chen SB, Xiao H (2013) REE geochemistry of Mengya'a lead-zinc deposit in Tibet. J Guilin University of Technol 33(2):230–238 (**in Chinese with English abstract**)

Zhai DG, Liu JJ, Zhang HY, Wang JP, Su L, Yang XA, Wu SH (2014) Origin of oscillatory zoned garnets from the Xieertala Fe–Zn skarn deposit, northern China: in situ LA–ICP–MS evidence. Lithos 190:279–291

Zheng YY, Wang BS, Fan ZH, Zhang HP (2002) Analysis of tectonic evolution in the eastern section of the gangdise moutains, Tibet and the metallogenic poten tialities of copper gold poly metal. Geol Sci Technol Inf 21:55–60 (**in Chinese with English abstract**)

Zhu DC, Mo XX, Zhao ZD, Xu JF, Zhou CY, Sun CG, Wang LQ, Chen HH, Dong GC, Zhou S (2008a) Zircon U-Pb geochronology of Zenong group volcanic roeks in Coqen area of the Gangdese, Tibet and tectonic significance. Acta Petrologica Sinica 24:401–412 (**in Chinese with English abstract**)

Zhu DC, Pan GT, Wang LQ, Mo XX, Zhao ZD, Zhou CY, Liao ZL, Dong GC, Yuan SH (2008b) Tempo-spatial variations of Mesozoic magmatic rocks in the Gangdise belt, Tibet, China, with a discussion of geodynamic setting-related issues. Geol Bull China 27:1535–1550 (**in Chinese with English abstract**)

Zhu DC, Zhao ZD, Niu YL, Wang Q, Dilek Y, Guan Q, Liu YS, Mo XX (2011) Tracing the provenance of inherited zircons from peraluminous granites in the Lhasa Terrane and its paleogeographic implications. Acta Petrologica Sinica 27:1917–1930 (**in Chinese with English abstract**)